

Incorporating Arbitrary Matrix Group Equivariance into KANs

Lexiang Hu¹ Yisen Wang^{1,2} Zhouchen Lin^{1,2,3}

Abstract

Kolmogorov-Arnold Networks (KANs) have seen great success in scientific domains thanks to spline activation functions, becoming an alternative to Multi-Layer Perceptrons (MLPs). However, spline functions may not respect symmetry in tasks, which is crucial prior knowledge in machine learning. In this paper, we propose Equivariant Kolmogorov-Arnold Networks (EKAN), a method for incorporating arbitrary matrix group equivariance into KANs, aiming to broaden their applicability to more fields. We first construct gated spline basis functions, which form the EKAN layer together with equivariant linear weights, and then define a lift layer to align the input space of EKAN with the feature space of the dataset, thereby building the entire EKAN architecture. Compared with baseline models, EKAN achieves higher accuracy with smaller datasets or fewer parameters on symmetry-related tasks, such as particle scattering and the three-body problem, often reducing test MSE by several orders of magnitude. Even in non-symbolic formula scenarios, such as top quark tagging with three jet constituents, EKAN achieves comparable results with state-of-the-art equivariant architectures using fewer than 40% of the parameters, while KANs do not outperform MLPs as expected.

1. Introduction

Kolmogorov-Arnold Networks (KANs) (Liu et al., 2024b;a) are a novel type of neural network inspired by the Kolmogorov-Arnold representation theorem (Tikhomirov, 1991; Braun & Griebel, 2009), which offers an alternative to Multi-Layer Perceptrons (MLPs) (Haykin, 1998; Cybenko, 1989; Hornik et al., 1989). Unlike MLPs, which utilize fixed activation functions on nodes, KANs employ learnable

activation functions on edges, replacing the linear weight parameters entirely with univariate functions parameterized as splines (De Boor & De Boor, 1978). On the other hand, each layer of KANs can be viewed as spline basis functions followed by a linear layer (Dhiman, 2024). This architecture allows KANs to achieve better accuracy in symbolic formula representation tasks compared with MLPs, particularly in function fitting and scientific applications. Subsequent works based on KANs have demonstrated superior performance in other areas, such as sequential data (Vaca-Rubio et al., 2024; Genet & Inzirillo, 2024b;a; Xu et al., 2024), graph data (Bresson et al., 2024; De Carlo et al., 2024; Kiamari et al., 2024; Zhang & Zhang, 2024), image data (Cheon, 2024b;a; Azam & Akhtar, 2024; Li et al., 2024a; Seydi, 2024; Bodner et al., 2024), and so on.

However, KANs themselves perform poorly on non-symbolic formula representation tasks (Yu et al., 2024). One reason for this is that splines struggle to respect data type and symmetry, both of which play important roles in machine learning. Many recent works utilize symmetry in data to design network architectures, achieving better efficiency and generalization on specific tasks. For example, Convolutional Neural Networks (CNNs) (LeCun et al., 1989) and Group equivariant Convolutional Neural Networks (GCNNs) (Cohen & Welling, 2016a) leverage translational and rotational symmetries in image data, while DeepSets (Zaheer et al., 2017) and equivariant graph networks (Maron et al., 2018; Keriven & Peyré, 2019; Satorras et al., 2021) exploit the permutation symmetry in set and graph data. Equivariant Multi-Layer Perceptrons (EMLP) (Finzi et al., 2021) propose a general method that allows MLPs to be equivariant with respect to arbitrary matrix groups for specific data types, thereby unifying the aforementioned specialized network architectures.

Inspired by these equivariant architectures, we propose Equivariant Kolmogorov-Arnold Networks (EKAN), which embed matrix group equivariance into KANs. By specifying the data type and symmetry, EKAN can serve as a general framework for applying KANs to various areas. In Section 2, we introduce the preliminary knowledge of group theory. In Section 3, we summarize related works. In Section 4, we construct a layer of EKAN. We add gate scalars to the input and output space of each layer, and define gated spline basis functions between the input and post-activation space. To

¹State Key Lab of General AI, School of Intelligence Science and Technology, Peking University ²Institute for Artificial Intelligence, Peking University ³Pazhou Laboratory (Huangpu), Guangzhou, Guangdong, China. Correspondence to: Zhouchen Lin <zlin@pku.edu.cn>.

ensure equivariance when linearly combining gated basis functions, we construct the equivariant constraint and solve for the equivariant linear weights. In Section 5, we build the entire EKAN architecture. We insert a lift layer before the first layer and discard the gate scalars from the output of the final layer, so that the input and output space of EKAN can be consistent with the original dataset. In Section 6, we evaluate EKAN on tasks with known symmetries. We show that EKAN can achieve higher accuracy than baseline models with smaller datasets or fewer parameters. In Section 7, we conclude this work. In Figure 1, we compare the architectures of KANs and EKAN.

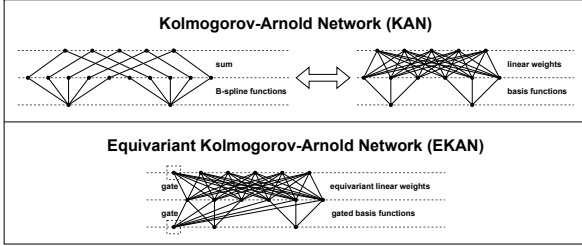


Figure 1. Comparison of the architectures of Kolmogorov-Arnold Networks (KANs) and Equivariant Kolmogorov-Arnold Networks (EKAN).

In summary, our contributions are as follows: (1) We propose EKAN, an architecture that makes KANs equivariant to matrix groups. To our knowledge, EKAN is the first attempt to combine equivariance with KANs, and we expect that it can serve as a general framework to broaden the applicability of KANs to more areas. (2) We specify the space structures of the EKAN Layer and define gated spline basis functions. We theoretically prove that gated basis functions can ensure equivariance between the gated input space and the post-activation space. Then, we insert a lift layer to preprocess the raw input feature, which aligns the input space of EKAN with the feature space of the dataset. (3) Experiments on tasks with matrix group equivariance, such as particle scattering and the three-body problem, demonstrate that EKAN often significantly outperforms baseline models, even with smaller datasets or fewer parameters. In the task of non-symbolic formula representation, where KANs are not proficient, such as top quark tagging with three jet constituents, EKAN can still achieve comparable results with state-of-the-art equivariant architectures while using fewer than 40% of the parameters.

2. Background

Before presenting related works and our method, we first introduce some preliminary knowledge of group theory.

Groups and generators. The matrix group \tilde{G} is a subgroup of the general linear group $GL(n)$, which consists of $n \times n$ invertible matrices. Each group element $g \in \tilde{G}$ can be decomposed into a continuous and a finite component $g = g_1 g_2$. We can obtain the continuous component g_1 from a Lie algebra element $A \in \mathfrak{g}$ through the exponential map $\exp : \mathfrak{g} \rightarrow \tilde{G}$, i.e., $g_1 = \exp(A) = \sum_{k=0}^{\infty} \frac{A^k}{k!}$. Representing the space where the Lie algebra resides as a basis $\{A_i\}_{i=1}^D$, we have $g_1 = \exp\left(\sum_{i=1}^D \alpha_i A_i\right)$. On the other hand, the finite component g_2 can be generated by a set of group elements $\{h_i\}_{i=1}^M$ and their inverses $h_{-k} = h_k^{-1}$, formally speaking $g_2 = \prod_{i=1}^N h_{k_i}$. Overall, we can express the matrix group element as:

$$g = \exp\left(\sum_{i=1}^D \alpha_i A_i\right) \prod_{i=1}^N h_{k_i}, \quad (1)$$

where $\{A_i\}_{i=1}^D$ are called infinitesimal generators and $\{h_i\}_{i=1}^M$ are called discrete generators. We introduce common matrix groups and their generators in Appendix A.

Group representations. The group representation $\rho_V : \tilde{G} \rightarrow GL(m)$ maps group elements to $m \times m$ invertible matrices, which describes how group elements act on the vector space $V = \mathbb{R}^m$ through linear transformations. For $g_1, g_2 \in \tilde{G}$ it satisfies $\rho_V(g_1 g_2) = \rho_V(g_1) \rho_V(g_2)$. Similarly, the Lie algebra representation is defined as $d\rho_V : \mathfrak{g} \rightarrow \mathfrak{gl}(m)$, and for $A_1, A_2 \in \mathfrak{g}$, we have $d\rho_V(A_1 + A_2) = d\rho_V(A_1) + d\rho_V(A_2)$. We can relate the Lie group representation to the Lie algebra representation through the exponential map. Specifically, for $A \in \mathfrak{g}$, $\rho_V(\exp(A)) = \exp(d\rho_V(A))$ holds. Then, combining with Equation (1), the matrix group representation can be written as:

$$\rho_V(g) = \exp\left(\sum_{i=1}^D \alpha_i d\rho_V(A_i)\right) \prod_{i=1}^N \rho_V(h_{k_i}). \quad (2)$$

We can construct the complex vector space from the base vector space using the dual (*), direct sum (\oplus), and tensor product (\otimes) operations. To give a concrete example, let V_1 and V_2 be base vector spaces. The multi-channel vector space, matrix space and parameter space of the linear mapping $V_1 \rightarrow V_2$ can be represented as $V_1 \oplus V_2$, $V_1 \otimes V_2$, and $V_2 \otimes V_1^*$, respectively. In general, given a matrix group \tilde{G} , we can normalize a vector space U into a polynomial-like form with respect to the base vector space V of \tilde{G} (the space where the group representation is the identity mapping $\rho_V(g) = g$; intuitively, the transformation matrix is the matrix group element itself):

$$U = \bigoplus_{a=1}^A T(p_a, q_a) = \bigoplus_{a=1}^A V^{p_a} \otimes (V^*)^{q_a}, \quad (3)$$

where $V^{p_a} = \underbrace{V \otimes V \otimes \dots \otimes V}_{p_a}$ and $(V^*)^{q_a} = \underbrace{V^* \otimes V^* \otimes \dots \otimes V^*}_{q_a}$. Its group representation and Lie algebra representation can be generated by the following rules:

$$\begin{cases} \rho_{V^*}(g) = \rho_V(g^{-1})^\top, \\ \rho_{V_1 \oplus V_2}(g) = \rho_{V_1}(g) \oplus \rho_{V_2}(g), \\ \rho_{V_1 \otimes V_2}(g) = \rho_{V_1}(g) \otimes \rho_{V_2}(g), \\ d\rho_{V^*}(A) = -d\rho_V(A)^\top, \\ d\rho_{V_1 \oplus V_2}(A) = d\rho_{V_1}(A) \oplus d\rho_{V_2}(A), \\ d\rho_{V_1 \otimes V_2}(A) = d\rho_{V_1}(A) \boxplus d\rho_{V_2}(A), \end{cases} \quad (4)$$

where \oplus is the direct sum, \otimes is the Kronecker product, and \boxplus is the Kronecker sum.

Equivariance and invariance. The symmetry can be divided into equivariance and invariance, meaning that when a transformation is applied to the input space, the output space either transforms in the same way or remains unchanged. Formally, given a group \tilde{G} , a function $f : U_i \rightarrow U_o$ is equivariant if:

$$\forall g \in \tilde{G}, v_i \in U_i : \rho_o(g)f(v_i) = f(\rho_i(g)v_i), \quad (5)$$

where ρ_i and ρ_o are group representations of U_i and U_o , respectively. Specifically, when $\rho_o(g) = I$, the function f is invariant.

3. Related work

Equivariant networks. Equivariant networks have gained significant attention in recent years due to their ability to respect and leverage symmetries in data. GCNNs (Cohen & Welling, 2016a) embed discrete group equivariance into traditional CNNs through group convolutions. Steerable CNNs (Cohen & Welling, 2016b) introduce steerable filters, which provide a more flexible and efficient way to achieve equivariance compared with GCNNs. Subsequently, SFCNNs (Weiler et al., 2018b) and E(2)-equivariant steerable CNNs (Weiler & Cesa, 2019) extend GCNNs and steerable CNNs to continuous group equivariance, while 3D Steerable CNNs (Weiler et al., 2018a) extend these models to 3D volumetric data. On the other hand, some works use partial differential operators (PDOs) to construct equivariant networks (Shen et al., 2020; 2021; 2022; He et al., 2022; Li et al., 2024b). Furthermore, equivariant self-supervised learning (Wang et al., 2020b; Dangovski et al., 2021; Lee et al., 2022; Garrido et al., 2023; Gupta et al., 2023) has also achieved outstanding results. Based on these theoretical frameworks, equivariant networks are widely applied in various fields, such as mathematics (Zhao et al., 2022), physics (Wang et al., 2020a), biochemistry (Bekkers et al., 2018; Winkels & Cohen, 2019; Graham et al., 2020), and others.

EMLP (Finzi et al., 2021) embeds matrix group equivariance into MLPs layerwise, which we discuss in detail in Appendix B.

Kolmogorov-Arnold Networks (KANs). KANs (Liu et al., 2024b;a) place learnable activation functions on the edges and then sum them to obtain the output nodes, replacing the fixed activation functions applied to the output nodes of linear layers in MLPs. Formally, the l -th KAN layer can be expressed as:

$$x_{l+1,j} = \sum_{i=1}^{n_l} \phi_{l,j,i}(x_{l,i}), \quad j = 1, \dots, n_{l+1}, \quad (6)$$

where n_l is the number of nodes in the l -th layer, $x_{l,i}$ is the value of the i -th node in the l -th layer, and $\phi_{l,j,i}$ is the activation function that connects $x_{l,i}$ to $x_{l+1,j}$. In practice, $\phi_{l,j,i}$ consists of a spline function and a silu function. The spline basis functions are determined by grids, which are updated based on the input samples. Then we can write the post-activation of $\phi_{l,j,i}$ as $\phi_{l,j,i}(x_{l,i}) = \sum_{b=0}^{G+k-1} w_{l,j,i,b} B_{l,i,b}(x_{l,i}) + w_{l,j,i,G+k} \text{silu}(x_{l,i})$, where G , k , and $B_{l,i,b}$ represent the number of grid intervals, the order, and the b -th basis function of splines at node $x_{l,i}$, respectively. Therefore, the KAN layer can be viewed as spline basis functions $B_{l,i,b}$ and a silu function, followed by a linear layer with $w_{l,j,i,b}$ as parameters (Dhiman, 2024):

$$x_{l+1,j} = \sum_{i=1}^{n_l} \left[\sum_{b=0}^{G+k-1} w_{l,j,i,b} B_{l,i,b}(x_{l,i}) + w_{l,j,i,G+k} \text{silu}(x_{l,i}) \right], \quad j = 1, \dots, n_{l+1}. \quad (7)$$

4. EKAN layer

In this section, we construct the EKAN layer, which is equivariant with respect to the matrix group \tilde{G} . First, we define the space structures and explain their relationships. Then, we introduce gated basis functions and equivariant linear weights, which together form a layer of EKAN. We summarize the space structures and network architecture of the EKAN layer in Figure 2.

4.1. Space structures

A key aspect of equivariant networks is how group elements act on the feature space. Therefore, unlike conventional networks, which only focus on the dimensions of the feature space, equivariant networks need to further clarify the structure of the feature space. For example, for the group $\text{SO}(2)$, two feature spaces $U_1 = V \oplus V = \mathbb{R}^2 \oplus \mathbb{R}^2$ and $U_2 = V \otimes V = \mathbb{R}^2 \otimes \mathbb{R}^2$ have different group representations ρ_{U_1} and ρ_{U_2} , but conventional networks treat them as the same space $U = \mathbb{R}^4$.

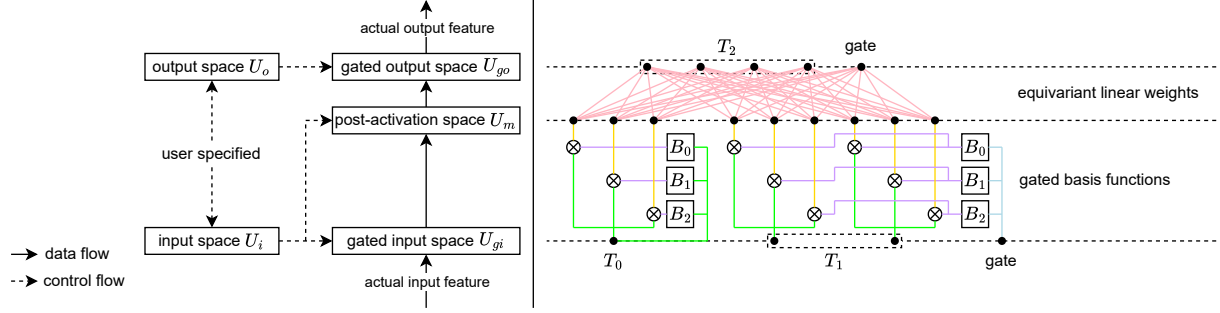


Figure 2. (Left) The space structures of the EKAN layer and their relationships. (Right) The architecture of the EKAN layer, which consists of gated basis functions and equivariant linear weights.

We specify the input space and the output space of EKAN layer as U_i and U_o , respectively. Their structures can be normalized into the form of Equation (3). In particular, for ease of later discussion, we extract the scalar space terms $T_0 = T(0, 0)$ and rewrite them as:

$$\begin{cases} U_i = c_i T_0 \oplus \left[\bigoplus_{a=1}^{A_i} T(p_{i,a}, q_{i,a}) \right], \\ U_o = c_o T_0 \oplus \left[\bigoplus_{a=1}^{A_o} T(p_{o,a}, q_{o,a}) \right], \end{cases} \quad (8)$$

where $p_{i,a}, q_{i,a}, p_{o,a}, q_{o,a}, c_i, c_o, A_i, A_o \in \mathbb{N}$, $p_{i,a}^2 + q_{i,a}^2 > 0$, $p_{o,a}^2 + q_{o,a}^2 > 0$, and $cT_0 = \underbrace{T_0 \oplus T_0 \oplus \dots \oplus T_0}_c$.

We have to emphasize that the actual input/output feature does not lie within U_i/U_o . To align with gated basis functions, we add a gate scalar T_0 to each non-scalar term $T(p_{i,a}, q_{i,a})/T(p_{o,a}, q_{o,a})$ in U_i/U_o to obtain the actual input/output space. The mechanism behind this approach will be discussed in detail in Section 4.2. We denote this actual input/output space as the gated input/output space U_{gi}/U_{go} :

$$\begin{cases} U_{gi} = c_i T_0 \oplus \left[\bigoplus_{a=1}^{A_i} T(p_{i,a}, q_{i,a}) \right] \oplus A_i T_0, \\ U_{go} = c_o T_0 \oplus \left[\bigoplus_{a=1}^{A_o} T(p_{o,a}, q_{o,a}) \right] \oplus A_o T_0. \end{cases} \quad (9)$$

As shown in Equation (7), we split the KAN layer into basis functions and linear weights. From this perspective, we correspondingly construct gated basis functions and equivariant linear weights to form the EKAN layer. We refer to the space where the activation values reside after gated basis functions and before equivariant linear weights as the post-activation space U_m . The structure of U_m depends on U_i , which we will elaborate on in Section 4.2.

We summarize the aforementioned space structures and their relationships in Figure 2 (Left). The user first specifies the input space U_i and the output space U_o for the EKAN layer. Then the gated input space U_{gi} and the post-activation space U_m are calculated based on U_i , and the gated output space U_{go} is calculated based on U_o . The actual input feature in

U_{gi} passes through gated basis functions to obtain the activation value in U_m , which then passes through equivariant linear weights to obtain the actual output feature in U_{go} .

4.2. Gated basis functions

Since spline basis functions are nonlinear and have relatively complex iterative forms, directly solving the equivariance constraint in Equation (5) is quite challenging. Recently, gating mechanisms have been widely used in various areas, not only in language models to improve performance (Dauphin et al., 2017; Shazeer, 2020; Gu & Dao, 2023) but also in the design of equivariant networks (Weiler et al., 2018a; Finzi et al., 2021). Inspired by this, we propose gated basis functions to make the basis functions in KANs (spline basis functions and the silu function) equivariant. Suppose that the input feature $v_{gi} \in U_{gi}$ can be decomposed according to the space structure shown in Equation (9):

$$v_{gi} = \left(\bigoplus_{a=1}^{c_i} s_{i,a} \right) \oplus \left(\bigoplus_{a=1}^{A_i} v_{i,a} \right) \oplus \left(\bigoplus_{a=1}^{A_i} s'_{i,a} \right), \quad (10)$$

where $s_{i,a}, s'_{i,a} \in T_0$ and $v_{i,a} \in T(p_{i,a}, q_{i,a})$. For the non-scalar term $v_{i,a}$, we apply the basis functions to the corresponding gate scalar $s'_{i,a}$ and then multiply the result by $v_{i,a}$. For the scalar term $s_{i,a}$, we consider it as its own gate scalar, which is equivalent to applying basis functions element-wise to $s_{i,a}$. Formalizing the above content, the post-activation value $v_m \in U_m$ can be written as:

$$v_m = \bigoplus_{b=0}^{G+k} v_{m,b}, \quad (11)$$

where

$$v_{m,b} = \begin{cases} \left[\bigoplus_{a=1}^{c_i} s_{i,a} B_b(s_{i,a}) \right] \oplus \left[\bigoplus_{a=1}^{A_i} v_{i,a} B_b(s'_{i,a}) \right], & b < G + k, \\ \left[\bigoplus_{a=1}^{c_i} s_{i,a} \text{silu}(s_{i,a}) \right] \oplus \left[\bigoplus_{a=1}^{A_i} v_{i,a} \text{silu}(s'_{i,a}) \right], & b = G + k. \end{cases} \quad (12)$$

Note that $v_{m,b} \in c_i T_0 \oplus \left[\bigoplus_{a=1}^{A_i} T(p_{i,a}, q_{i,a}) \right] = U_i$. Therefore, we obtain the structure of the post-activation space U_m :

$$U_m = (G + k + 1)U_i. \quad (13)$$

The following theorem guarantees the equivariance between the gated input space and the post-activation space (see Appendix C for proof).

Theorem 4.1. *Given a matrix group \tilde{G} , the gated input space U_{gi} and the post-activation space U_m can be expressed in the forms of Equations (9) and (13), respectively. The function $f : U_{gi} \rightarrow U_m$ is defined by Equations (10) to (12), that is, $v_m = f(v_{gi})$. Then, f is equivariant:*

$$\forall g \in \tilde{G}, v_{gi} \in U_{gi} : \quad \rho_m(g)f(v_{gi}) = f(\rho_{gi}(g)v_{gi}), \quad (14)$$

where ρ_{gi} and ρ_m are group representations of U_{gi} and U_m , respectively.

4.3. Equivariant linear weights

The output feature $v_{go} \in U_{go}$ is obtained by a linear combination of the post-activation value $v_m \in U_m$. Let $U_i = \mathbb{R}^{d_i}$ and $U_{go} = \mathbb{R}^{d_{go}}$, then Equation (13) indicates that $U_m = \mathbb{R}^{(G+k+1)d_i}$. The linear weight matrix $W \in \mathbb{R}^{d_{go} \times (G+k+1)d_i}$ can be partitioned as $W = [W_0 \ W_1 \ \dots \ W_{G+k}]$, where $W_b \in \mathbb{R}^{d_{go} \times d_i}$. Combining with Equation (11), we have:

$$v_{go} = Wv_m = \sum_{b=0}^{G+k} W_b v_{m,b}. \quad (15)$$

To ensure the equivariance between the post-activation space and the gated output space, we obtain:

$$\forall g \in \tilde{G}, v_m \in U_m : \quad \rho_{go}(g)Wv_m = W\rho_m(g)v_m, \quad (16)$$

where ρ_{go} is the group representation of U_{go} . Using the structure of U_m shown in Equation (13) and applying the rules from Equation (4), we can derive that $\rho_m(g) = \bigoplus_{b=0}^{G+k} \rho_i(g)$, where ρ_i is the group representation of U_i . Therefore, from Equation (11), we have $\rho_m(g)v_m = \bigoplus_{b=0}^{G+k} \rho_i(g)v_{m,b}$. Then Equation (16) can be written as:

$$\forall g \in \tilde{G}, \{v_{m,b}\}_{b=0}^{G+k} \in U_i : \quad \sum_{b=0}^{G+k} \rho_{go}(g)W_b v_{m,b} = \sum_{b=0}^{G+k} W_b \rho_i(g)v_{m,b}. \quad (17)$$

The coefficients of each term in $\{v_{m,b}\}_{b=0}^{G+k}$ are equal:

$$\forall g \in \tilde{G}, b \in \{0, 1, \dots, G+k\} : \quad \rho_{go}(g)W_b = W_b \rho_i(g). \quad (18)$$

Flattening the linear weight blocks $\{W_b\}_{b=0}^{G+k}$ into vectors, we obtain:

$$\forall g \in \tilde{G}, b \in \{0, 1, \dots, G+k\} : \quad \rho_{go,i}(g)\text{vec}(W_b) = \text{vec}(W_b), \quad (19)$$

where $\rho_{go,i} = \rho_{go} \otimes \rho_i^*$ is the group representation of $U_{go} \otimes U_i^*$. We use the same method as EMLP (Finzi et al., 2021) to solve for the equivariant basis Q and equivariant projector $P = QQ^\top$ of $\text{vec}(W_b)$. Similar to the transition from Equation (27) to Equation (28) (in Appendix B), we decompose the group representation $\rho_{go,i}(g)$ into discrete and infinitesimal generators to obtain the following constraint:

$$\forall b \in \{0, 1, \dots, G+k\} : \quad C\text{vec}(W_b) = \begin{bmatrix} d\rho_{go,i}(A_1) \\ \vdots \\ d\rho_{go,i}(A_D) \\ \rho_{go,i}(h_1) - I \\ \vdots \\ \rho_{go,i}(h_M) - I \end{bmatrix} \text{vec}(W_b) = 0. \quad (20)$$

Note that the equivariant linear weight blocks $\{W_b\}_{b=0}^{G+k}$ lie in the same subspace, which corresponds to the nullspace of the coefficient matrix C . We can obtain it via SVD.

We summarize the architecture of the EKAN layer in Figure 2 (Right). In this example, the EKAN layer is equivariant with respect to a 2-dimensional matrix group \tilde{G} (such as the $\text{SO}(2)$ group). The user specifies the input space $U_i = T_0 \oplus T_1$ (where we abbreviate $T(p, 0) = V^p$ as T_p), which represents a scalar space and a vector space, and specifies the output space $U_o = T_2$, which represents a matrix space. Then, the gated input space $U_{gi} = T_0 \oplus T_1 \oplus T_0$ and the gated output space $U_{go} = T_2 \oplus T_0$ each add a gate scalar to the vector space T_1 and the matrix space T_2 . The basis functions are applied to the gate scalars of T_0 (itself) and T_1 , which are then multiplied by the original terms to obtain the post-activation space $U_m = 3U_i$. The linear weights $W \in \mathbb{R}^{5 \times 9}$ between U_m and U_{go} are within the subspace determined by Equation (20) to ensure equivariance. Similar to KANs (Liu et al., 2024b), EKAN updates grids based on the input activations, which we discuss in detail in Appendix D.

5. EKAN architecture

In this section, we construct the entire EKAN architecture. The main body of EKAN is composed of stacked EKAN layers. The output space of the l -th layer serves as the input space of the $(l+1)$ -th layer, which we refer to as the latent space U_l . For the dataset, we usually know its data type, or in other words, how group elements act on it. To embed this prior knowledge into EKAN, we set the input space

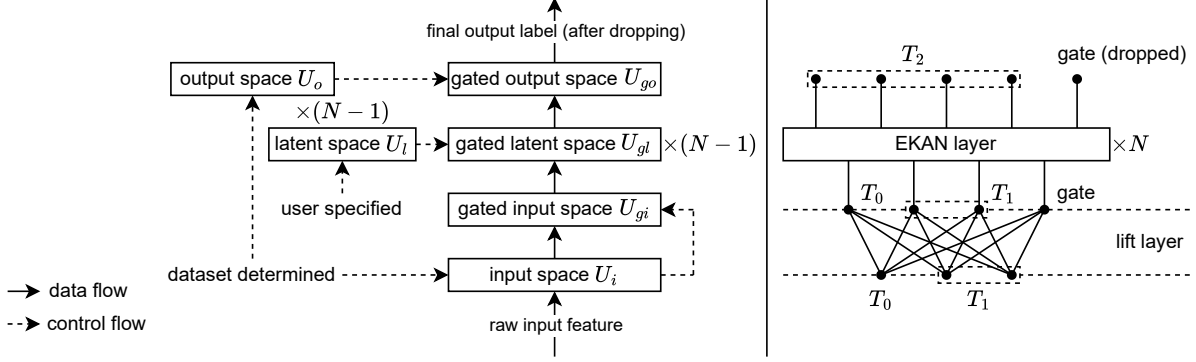


Figure 3. (Left) The space structures of EKAN and their relationships. (Right) The EKAN architecture, which consists of a lift layer and stacked EKAN layers.

of the first layer as the feature space of the dataset U_i and the output space of the final layer as the label space of the dataset U_o .

However, the actual input/output features of the EKAN layer stack lie in U_{gi}/U_{go} . Therefore, we need to add extensions to align the network with the dataset. First, the gate scalars of the actual output feature are directly dropped to obtain the final output label of EKAN, which resides in U_o . Then, we add a lift layer before the first layer to preprocess the raw input feature of EKAN, which is essentially an equivariant linear layer between U_i and U_{gi} (see Section 4.3).

We summarize the space structures and network architecture of EKAN in Figure 3. The space structures of EKAN can be analogous to the dimensions of a conventional network. The user specifies the latent space U_l of EKAN, which corresponds to specifying the hidden dimension in a conventional network. The input space U_i and the output space U_o are determined by the dataset, similar to how the input and output dimensions are defined in a conventional network. In the concrete example, the feature space and label space of the dataset are $U_i = T_0 \oplus T_1$ and $U_o = T_2$, respectively. After passing through the lift layer, a new gate scalar is added to the raw input feature for T_1 , resulting in the actual input feature $U_{gi} = T_0 \oplus T_1 \oplus T_0$ for the first EKAN layer. The gate scalar in the actual output space $U_{go} = T_2 \oplus T_0$ of the last EKAN layer is dropped to obtain the final output label.

6. Experiments

In this section, we evaluate the performance of EKAN on regression and classification tasks with known symmetries. Compared with general models such as MLPs, KANs, and equivariant architectures like EMLP (Finzi et al., 2021) and CGENN (Ruhe et al., 2023), EKAN achieves lower test loss and higher test accuracy with smaller datasets or fewer parameters.

6.1. Particle scattering

In electron-muon scattering, we can observe the four-momenta of the incoming electron, incoming muon, outgoing electron, and outgoing muon, denoted as $q^\mu, p^\mu, \tilde{q}^\mu, \tilde{p}^\mu \in \mathbb{R}^4$, respectively. We aim to predict the matrix element, which is proportional to the cross-section (Finzi et al., 2021): $|\mathcal{M}|^2 \propto [p^\mu \tilde{p}^\nu - (p^\alpha \tilde{p}_\alpha - p^\alpha p_\alpha) g^{\mu\nu}] [q_\mu \tilde{q}_\nu - (q^\alpha \tilde{q}_\alpha - q^\alpha q_\alpha) g_{\mu\nu}]$. According to Einstein’s summation convention, in a monomial, if an index appears once as a superscript and once as a subscript, it indicates summation over that index. The metric tensor is given by $g_{\mu\nu} = g^{\mu\nu} = \text{diag}(1, -1, -1, -1)$, and $a_\mu = g_{\mu\nu} a^\nu = (a^0, -a^1, -a^2, -a^3)$. The matrix element is invariant under Lorentz transformations. In other words, this task exhibits $O(1, 3)$ invariance (see Appendix A.2 for more details), with the feature space $U_i = 4T_1$ and the label space $U_o = T_0$.

We embed the group $O(1, 3)$ and its subgroups $SO^+(1, 3)$ and $SO(1, 3)$ equivariance into EKAN. Models are evaluated on synthetic datasets with different training set sizes, which are generated by sampling $q^\mu, p^\mu, \tilde{q}^\mu, \tilde{p}^\mu \sim \mathcal{N}(0, \frac{1}{4^2})$. Both EKAN and KAN have the depth of $L = 2$, the spline order of $k = 3$, and grid intervals of $G = 3$. Although the lift layer increases the parameter overhead, we set the width of the middle layer in EKAN to $n_1 = 1000$ (shape as $[16, 1000, 1]$), and the software will automatically calculate the appropriate feature space structure based on the user-specified dimension), and set the width of the middle layer in KAN to $n_1 = 3840$ (shape as $[16, 3840, 1]$) to keep the parameter count similar. Both EMLP and MLP have the depth of $L = 4$ and the middle layer width of $n_1 = n_2 = n_3 = 384$ (shape as $[16, 384, 384, 384, 1]$). In these settings, EKAN (435k) has fewer parameters than EMLP (450k) and KAN (461k). We provide more implementation details in Appendix E.1.

Table 1. Test MSE of different models on the particle scattering dataset with different training set sizes. We present the results in the format of mean \pm std.

Models	Training set size				
	10^2	$10^{2.5}$	10^3	$10^{3.5}$	10^4
MLP	$(7.33 \pm 0.01) \times 10^{-1}$	$(6.97 \pm 0.09) \times 10^{-1}$	$(3.64 \pm 0.30) \times 10^{-1}$	$(5.04 \pm 0.37) \times 10^{-2}$	$(1.66 \pm 0.07) \times 10^{-2}$
MLP + augmentation	$(1.90 \pm 0.22) \times 10^{-1}$	$(3.97 \pm 0.52) \times 10^{-2}$	$(1.25 \pm 0.08) \times 10^{-2}$	$(1.08 \pm 0.03) \times 10^{-2}$	$(1.34 \pm 0.22) \times 10^{-2}$
EMLP-SO ⁺ (1, 3)	$(1.27 \pm 0.35) \times 10^{-2}$	$(2.21 \pm 0.56) \times 10^{-3}$	$(3.30 \pm 0.86) \times 10^{-4}$	$(2.24 \pm 0.55) \times 10^{-4}$	$(1.99 \pm 0.33) \times 10^{-4}$
EMLP-SO(1, 3)	$(1.47 \pm 0.91) \times 10^{-2}$	$(2.58 \pm 0.25) \times 10^{-3}$	$(3.69 \pm 1.25) \times 10^{-4}$	$(2.73 \pm 0.30) \times 10^{-4}$	$(2.12 \pm 0.15) \times 10^{-4}$
EMLP-O(1, 3)	$(8.88 \pm 2.51) \times 10^{-3}$	$(1.95 \pm 0.18) \times 10^{-3}$	$(3.30 \pm 0.43) \times 10^{-4}$	$(2.66 \pm 0.66) \times 10^{-4}$	$(2.64 \pm 0.28) \times 10^{-4}$
KAN	$(6.70 \pm 1.35) \times 10^{-1}$	$(6.16 \pm 1.18) \times 10^{-1}$	$(3.46 \pm 0.15) \times 10^{-1}$	$(1.21 \pm 0.07) \times 10^{-1}$	$(2.57 \pm 0.08) \times 10^{-2}$
KAN + augmentation	$(5.98 \pm 0.67) \times 10^{-1}$	$(4.72 \pm 1.52) \times 10^{-1}$	$(9.07 \pm 2.36) \times 10^{-2}$	$(5.61 \pm 0.70) \times 10^{-2}$	$(1.58 \pm 0.06) \times 10^{-1}$
EKAN-SO ⁺ (1, 3) (Ours)	$(6.86 \pm 6.28) \times 10^{-3}$	$(1.85 \pm 1.75) \times 10^{-3}$	$(2.01 \pm 1.93) \times 10^{-5}$	$(1.93 \pm 1.11) \times 10^{-5}$	$(4.29 \pm 3.38) \times 10^{-6}$
EKAN-SO(1, 3) (Ours)	$(6.86 \pm 6.27) \times 10^{-3}$	$(1.85 \pm 1.75) \times 10^{-3}$	$(2.06 \pm 1.88) \times 10^{-5}$	$(2.17 \pm 1.51) \times 10^{-5}$	$(3.85 \pm 2.77) \times 10^{-6}$
EKAN-O(1, 3) (Ours)	$(7.77 \pm 5.85) \times 10^{-3}$	$(1.64 \pm 1.87) \times 10^{-3}$	$(2.85 \pm 3.09) \times 10^{-5}$	$(7.31 \pm 4.15) \times 10^{-6}$	$(3.81 \pm 2.83) \times 10^{-6}$

 Table 2. Test MSE of different models with different numbers of parameters on the three-body problem dataset. We present the results in the format of mean \pm std.

Models	Number of parameters				
	$10^{4.5}$	$10^{4.75}$	10^5	$10^{5.25}$	$10^{5.5}$
MLP	$(4.84 \pm 0.19) \times 10^{-3}$	$(4.70 \pm 0.30) \times 10^{-3}$	$(4.60 \pm 0.12) \times 10^{-3}$	$(4.17 \pm 0.24) \times 10^{-3}$	$(4.24 \pm 0.27) \times 10^{-3}$
MLP + augmentation	$(9.43 \pm 0.88) \times 10^{-3}$	$(9.65 \pm 0.54) \times 10^{-3}$	$(1.01 \pm 0.09) \times 10^{-2}$	$(9.89 \pm 0.65) \times 10^{-3}$	$(9.91 \pm 0.46) \times 10^{-3}$
EMLP-SO(2)	$(2.28 \pm 1.17) \times 10^{-3}$	$(6.87 \pm 5.29) \times 10^{-3}$	$(3.55 \pm 1.59) \times 10^{-3}$	$(2.01 \pm 1.09) \times 10^{-3}$	$(5.34 \pm 3.78) \times 10^{-3}$
EMLP-O(2)	$(7.72 \pm 8.71) \times 10^{-3}$	$(1.18 \pm 0.22) \times 10^{-3}$	$(1.42 \pm 1.86) \times 10^{-2}$	$(7.37 \pm 7.60) \times 10^{-3}$	$(1.37 \pm 0.07) \times 10^{-3}$
KAN	$(4.32 \pm 3.08) \times 10^{-1}$	$(2.21 \pm 0.65) \times 10^{-2}$	$(1.18 \pm 0.18) \times 10^{-2}$	$(1.23 \pm 0.34) \times 10^{-2}$	$(9.15 \pm 1.76) \times 10^{-3}$
KAN + augmentation	$(7.94 \pm 0.15) \times 10^{-3}$	$(7.15 \pm 0.24) \times 10^{-3}$	$(6.91 \pm 0.34) \times 10^{-3}$	$(6.88 \pm 0.06) \times 10^{-3}$	$(6.76 \pm 0.12) \times 10^{-3}$
EKAN-SO(2) (Ours)	$(1.12 \pm 0.13) \times 10^{-3}$	$(7.06 \pm 0.65) \times 10^{-4}$	$(6.09 \pm 0.27) \times 10^{-4}$	$(4.26 \pm 0.19) \times 10^{-4}$	$(4.84 \pm 0.68) \times 10^{-4}$
EKAN-O(2) (Ours)	$(1.48 \pm 0.37) \times 10^{-3}$	$(1.12 \pm 0.24) \times 10^{-3}$	$(7.91 \pm 0.52) \times 10^{-4}$	$(6.06 \pm 0.36) \times 10^{-4}$	$(6.02 \pm 0.88) \times 10^{-4}$

We repeat experiments with three different random seeds and report the mean \pm std of the test MSE in Table 1. The results of EMLP and MLP come from the original paper (Finzi et al., 2021) under the same settings. Although EMLP performs better than non-equivariant models, our EKAN with different group equivariance further surpasses it comprehensively, especially showing an orders-of-magnitude advantage on large datasets (training set size $\geq 10^3$). Moreover, our EKAN with just 10^3 training samples achieves approximately 10% of the test MSE of EMLP with 10^4 training samples.

6.2. Three-body problem

The study of the three-body problem on a plane (Greydanus et al., 2019) focuses on the motion of three particles, with their center of mass at the origin, under the influence of gravity. Their trajectories are chaotic and cannot be described by an analytical solution. Specifically, we observe the motion states of three particles over the past four time steps, denoted as $\{q_{i1}, p_{i1}, q_{i2}, p_{i2}, q_{i3}, p_{i3}\}_{i=t-4}^{t-1}$, and predict their motion states at time t , denoted as $\{q_{t1}, p_{t1}, q_{t2}, p_{t2}, q_{t3}, p_{t3}\}$. Here, $q_{ij} \in \mathbb{R}^2$ and $p_{ij} \in \mathbb{R}^2$ indicate the position and momentum coordinates of the j -th particle at time i , respectively. The dataset contains 30k training samples and 30k test samples. When the input motion states are simul-

taneously rotated by a certain angle or reflected along a specific axis, the output motion states should undergo the same transformation. Therefore, this task has O(2) equivariance (see Appendix A.1 for more details), with the feature space $U_i = 4 \times 6T_1 = 24T_1$ and the label space $U_o = 6T_1$.

We embed the group O(2) and its subgroup SO(2) equivariance into EKAN and EMLP. Both EKAN and KAN have the depth of $L = 2$, the spline order of $k = 3$, and grid intervals of $G = 3$, while both EMLP and MLP have the depth of $L = 4$. The number of parameters is controlled by adjusting the middle layer width N for comparison (the shape of EKAN and KAN is $[48, N, 12]$, while the shape of EMLP and MLP is $[48, N, N, N, 12]$). More implementation details can be found in Appendix E.2.

The mean \pm std of the test MSE over three runs with different random seeds are reported in Table 2. Our EKAN-SO(2) and EKAN-O(2) consistently outperform baseline models with the same number of parameters, often by orders of magnitude. Notably, our EKAN with $10^{4.5}$ parameters achieves comparable or even lower test MSE than baseline models with $10^{5.5}$ parameters, saving 90% of the parameter overhead.

Table 3. Test accuracy (%) of different models on the top quark tagging dataset with different training set sizes. We present the results in the format of mean \pm std.

Models	Training set size					Parameters
	10^2	$10^{2.5}$	10^3	$10^{3.5}$	10^4	
MLP	52.96 ± 0.21	54.31 ± 0.48	57.47 ± 0.32	62.72 ± 0.60	69.30 ± 1.03	83K
MLP + augmentation	52.72 ± 0.35	60.16 ± 0.41	61.29 ± 1.66	58.71 ± 1.37	59.45 ± 1.90	
EMLP-SO ⁺ (1, 3)	65.48 ± 1.21	72.59 ± 0.84	74.40 ± 0.26	76.34 ± 0.14	77.10 ± 0.02	133K
EMLP-SO(1, 3)	61.86 ± 5.92	73.09 ± 0.92	74.37 ± 0.17	76.46 ± 0.12	77.12 ± 0.04	
EMLP-O(1, 3)	62.66 ± 7.35	73.65 ± 1.01	74.22 ± 0.53	76.26 ± 0.05	77.12 ± 0.04	
KAN	49.89 ± 0.39	49.91 ± 0.43	49.89 ± 0.37	50.00 ± 0.02	49.84 ± 0.25	35K
KAN + augmentation	49.83 ± 0.28	50.09 ± 0.09	49.73 ± 0.40	50.02 ± 0.01	50.27 ± 0.67	
CGENN	62.63 ± 2.24	68.74 ± 0.77	70.29 ± 1.29	75.10 ± 0.47	77.05 ± 0.03	85K
EKAN-SO ⁺ (1, 3) (Ours)	71.92 ± 0.88	73.98 ± 0.39	76.15 ± 0.11	76.69 ± 0.08	76.93 ± 0.02	34K
EKAN-SO(1, 3) (Ours)	70.49 ± 2.85	73.96 ± 0.37	76.15 ± 0.11	76.69 ± 0.08	76.93 ± 0.02	
EKAN-O(1, 3) (Ours)	71.68 ± 1.21	73.95 ± 0.36	76.15 ± 0.11	76.69 ± 0.07	76.93 ± 0.03	

6.3. Top quark tagging

The research on top quark tagging (Kasieczka et al., 2019) involves classifying hadronic tops from the QCD background. In particle collision experiments, top quark decays or other events produce several jet constituents. We observe the four-momenta $p_1^\mu, p_2^\mu, p_3^\mu \in \mathbb{R}^4$ of the three jet constituents with the highest transverse momentum p_T , and predict the event label (1 for top, 0 for QCD). The category of the event will not change when all jet constituents undergo the same Lorentz transformation. Consequently, this task possesses $O(1, 3)$ invariance (see Appendix A.2 for more details), with the feature space $U_i = 3T_1$ and the label space $U_o = T_0$.

Similar to particle scattering, we embed the group $O(1, 3)$ and its subgroups $SO^+(1, 3)$ and $SO(1, 3)$ equivariance into EKAN and EMLP. Furthermore, we embed $O(1, 3)$ equivariance into CGENN (Ruhe et al., 2023). We sample training sets of different sizes from the original dataset for evaluation. Both EKAN and KAN have the depth of $L = 2$, the spline order of $k = 3$, and grid intervals of $G = 3$. We set the width of the middle layer in EKAN to $n_1 = 200$ (shape as $[12, 200, 1]$) and the width of the middle layer in KAN to $n_1 = 384$ (shape as $[12, 384, 1]$) to control the number of parameters. Both MLP, EMLP and CGENN have the depth of $L = 4$ and the middle layer width $n_1 = n_2 = n_3 = 200$ (shape as $[12, 200, 200, 200, 1]$). We apply the sigmoid function to the model’s output and use BCE as the loss function for binary classification. More implementation details are provided in Appendix E.3.

We report the mean \pm std of the test accuracy over three runs with different random seeds, as well as the number of parameters of the models in Table 3. Since we have not observed all the jet constituents, the relationship between

the labels and input features cannot be accurately expressed as an explicit function. In this case of non-symbolic formula representation, KAN cannot achieve higher accuracy with fewer parameters than MLP as expected. On the other hand, our EKAN achieves comparable results with EMLP and CGENN using fewer than 40% of the parameters, improving test accuracy by 0.23% \sim 6.44% on small datasets (training set size $< 10^4$), while decreasing by 0.19% on large datasets (training set size $= 10^4$).

7. Conclusion

To our knowledge, this work is the first attempt to combine equivariance and KANs. We view the KAN layer as a combination of spline functions and linear weights, and accordingly define the (gated) input space, post-activation space, and (gated) output space of the EKAN layer. Gated basis functions ensure the equivariance between the gated input space and the post-activation space, while equivariant linear weights guarantee the equivariance between the post-activation space and the gated output space. The prior work has demonstrated that “EMLP $>$ MLP” on tasks with symmetries and “KAN $>$ MLP” on symbolic formula representation tasks. Our experimental results further indicate that on symbolic formula representation tasks with symmetries, “EKAN $>$ EMLP” and “EKAN $>$ KAN”. Moreover, on non-symbolic formula representation tasks with symmetries, although it may be that “KAN $<$ MLP”, we show that “EKAN $>$ EMLP”. We expect that EKAN can become a general framework for applying KANs to more fields, such as computer vision and natural language processing, just as EMLP unifies classic works like CNNs and DeepSets.

Impact Statement

This paper presents work whose goal is to advance the field of Machine Learning. There are many potential societal consequences of our work, none which we feel must be specifically highlighted here.

References

- Azam, B. and Akhtar, N. Suitability of KANs for computer vision: A preliminary investigation. *arXiv preprint arXiv:2406.09087*, 2024.
- Bekkers, E. J., Lafarge, M. W., Veta, M., Eppenhof, K. A., Pluim, J. P., and Duits, R. Roto-translation covariant convolutional networks for medical image analysis. In *Medical Image Computing and Computer Assisted Intervention–MICCAI 2018: 21st International Conference, Granada, Spain, September 16-20, 2018, Proceedings, Part I*, pp. 440–448. Springer, 2018.
- Bodner, A. D., Tepsich, A. S., Spolski, J. N., and Pourteau, S. Convolutional Kolmogorov-Arnold networks. *arXiv preprint arXiv:2406.13155*, 2024.
- Braun, J. and Griebel, M. On a constructive proof of Kolmogorov’s superposition theorem. *Constructive approximation*, 30:653–675, 2009.
- Bresson, R., Nikolentzos, G., Panagopoulos, G., Chatzianastasis, M., Pang, J., and Vazirgiannis, M. KAGNNs: Kolmogorov-Arnold networks meet graph learning. *arXiv preprint arXiv:2406.18380*, 2024.
- Cheon, M. Demonstrating the efficacy of Kolmogorov-Arnold networks in vision tasks. *arXiv preprint arXiv:2406.14916*, 2024a.
- Cheon, M. Kolmogorov-Arnold network for satellite image classification in remote sensing. *arXiv preprint arXiv:2406.00600*, 2024b.
- Cohen, T. and Welling, M. Group equivariant convolutional networks. In *International Conference on Machine Learning*, pp. 2990–2999. PMLR, 2016a.
- Cohen, T. S. and Welling, M. Steerable CNNs. *arXiv preprint arXiv:1612.08498*, 2016b.
- Cybenko, G. Approximation by superpositions of a sigmoidal function. *Mathematics of control, signals and systems*, 2(4):303–314, 1989.
- Dangovski, R., Jing, L., Loh, C., Han, S., Srivastava, A., Cheung, B., Agrawal, P., and Soljačić, M. Equivariant contrastive learning. *arXiv preprint arXiv:2111.00899*, 2021.
- Dauphin, Y. N., Fan, A., Auli, M., and Grangier, D. Language modeling with gated convolutional networks. In *International Conference on Machine Learning*, pp. 933–941. PMLR, 2017.
- De Boor, C. and De Boor, C. *A practical guide to splines*, volume 27. springer New York, 1978.
- De Carlo, G., Mastropietro, A., and Anagnostopoulos, A. Kolmogorov-Arnold graph neural networks. *arXiv preprint arXiv:2406.18354*, 2024.
- Dhiman, V. KAN: Kolmogorov-Arnold networks: A review. 2024.
- Finzi, M., Welling, M., and Wilson, A. G. A practical method for constructing equivariant multilayer perceptrons for arbitrary matrix groups. In *International Conference on Machine Learning*, pp. 3318–3328. PMLR, 2021.
- Garrido, Q., Najman, L., and Lecun, Y. Self-supervised learning of split invariant equivariant representations. *arXiv preprint arXiv:2302.10283*, 2023.
- Genet, R. and Inzirillo, H. A temporal Kolmogorov-Arnold transformer for time series forecasting. *arXiv preprint arXiv:2406.02486*, 2024a.
- Genet, R. and Inzirillo, H. TKAN: Temporal Kolmogorov-Arnold networks. *arXiv preprint arXiv:2405.07344*, 2024b.
- Graham, S., Epstein, D., and Rajpoot, N. Dense steerable filter CNNs for exploiting rotational symmetry in histology images. *IEEE Transactions on Medical Imaging*, 39(12):4124–4136, 2020.
- Greydanus, S., Dzamba, M., and Yosinski, J. Hamiltonian neural networks. *Advances in Neural Information Processing Systems*, 32, 2019.
- Gu, A. and Dao, T. Mamba: Linear-time sequence modeling with selective state spaces. *arXiv preprint arXiv:2312.00752*, 2023.
- Gupta, S., Robinson, J., Lim, D., Villar, S., and Jegelka, S. Structuring representation geometry with rotationally equivariant contrastive learning. *arXiv preprint arXiv:2306.13924*, 2023.
- Haykin, S. *Neural networks: a comprehensive foundation*. Prentice Hall PTR, 1998.
- He, L., Chen, Y., Shen, Z., Yang, Y., and Lin, Z. Neural ePDOs: Spatially adaptive equivariant partial differential operator based networks. In *The Eleventh International Conference on Learning Representations*, 2022.

- Hornik, K., Stinchcombe, M., and White, H. Multilayer feedforward networks are universal approximators. *Neural networks*, 2(5):359–366, 1989.
- Kasieczka, G., Plehn, T., Thompson, J., and Ruszel, M. Top quark tagging reference dataset, March 2019. URL <https://doi.org/10.5281/zenodo.2603256>.
- Keriven, N. and Peyré, G. Universal invariant and equivariant graph neural networks. *Advances in Neural Information Processing Systems*, 32, 2019.
- Kiamari, M., Kiamari, M., and Krishnamachari, B. GKAN: Graph Kolmogorov-Arnold networks. *arXiv preprint arXiv:2406.06470*, 2024.
- LeCun, Y., Boser, B., Denker, J. S., Henderson, D., Howard, R. E., Hubbard, W., and Jackel, L. D. Backpropagation applied to handwritten zip code recognition. *Neural computation*, 1(4):541–551, 1989.
- Lee, J., Kim, B., and Cho, M. Self-supervised equivariant learning for oriented keypoint detection. In *Proceedings of the IEEE/CVF conference on computer vision and pattern recognition*, pp. 4847–4857, 2022.
- Li, C., Liu, X., Li, W., Wang, C., Liu, H., and Yuan, Y. U-KAN makes strong backbone for medical image segmentation and generation. *arXiv preprint arXiv:2406.02918*, 2024a.
- Li, Y., Qiu, Y., Chen, Y., He, L., and Lin, Z. Affine equivariant networks based on differential invariants. In *Proceedings of the IEEE/CVF Conference on Computer Vision and Pattern Recognition*, pp. 5546–5556, 2024b.
- Liu, Z., Ma, P., Wang, Y., Matusik, W., and Tegmark, M. KAN 2.0: Kolmogorov-Arnold networks meet science. *arXiv preprint arXiv:2408.10205*, 2024a.
- Liu, Z., Wang, Y., Vaidya, S., Ruehle, F., Halverson, J., Soljačić, M., Hou, T. Y., and Tegmark, M. KAN: Kolmogorov-Arnold networks. *arXiv preprint arXiv:2404.19756*, 2024b.
- Maron, H., Ben-Hamu, H., Shamir, N., and Lipman, Y. Invariant and equivariant graph networks. *arXiv preprint arXiv:1812.09902*, 2018.
- Ruhe, D., Brandstetter, J., and Forré, P. Clifford group equivariant neural networks. *Advances in Neural Information Processing Systems*, 36:62922–62990, 2023.
- Satorras, V. G., Hoogeboom, E., and Welling, M. E(n) equivariant graph neural networks. In *International Conference on Machine Learning*, pp. 9323–9332. PMLR, 2021.
- Seydi, S. T. Unveiling the power of wavelets: A wavelet-based Kolmogorov-Arnold network for hyperspectral image classification. *arXiv preprint arXiv:2406.07869*, 2024.
- Shazeer, N. GLU variants improve transformer. *arXiv preprint arXiv:2002.05202*, 2020.
- Shen, Z., He, L., Lin, Z., and Ma, J. PDO-eConvs: Partial differential operator based equivariant convolutions. In *International Conference on Machine Learning*, pp. 8697–8706. PMLR, 2020.
- Shen, Z., Shen, T., Lin, Z., and Ma, J. PDO-eS2CNNs: Partial differential operator based equivariant spherical CNNs. In *Proceedings of the AAAI Conference on Artificial Intelligence*, volume 35, pp. 9585–9593, 2021.
- Shen, Z., Hong, T., She, Q., Ma, J., and Lin, Z. PDO-s3DCNNs: Partial differential operator based steerable 3D CNNs. In *International Conference on Machine Learning*, pp. 19827–19846. PMLR, 2022.
- Tikhomirov, V. On the representation of continuous functions of several variables as superpositions of continuous functions of a smaller number of variables. In *Selected Works of AN Kolmogorov*, pp. 378–382. Springer, 1991.
- Vaca-Rubio, C. J., Blanco, L., Pereira, R., and Caus, M. Kolmogorov-Arnold networks (KANs) for time series analysis. *arXiv preprint arXiv:2405.08790*, 2024.
- Wang, R., Walters, R., and Yu, R. Incorporating symmetry into deep dynamics models for improved generalization. *arXiv preprint arXiv:2002.03061*, 2020a.
- Wang, Y., Zhang, J., Kan, M., Shan, S., and Chen, X. Self-supervised equivariant attention mechanism for weakly supervised semantic segmentation. In *Proceedings of the IEEE/CVF conference on computer vision and pattern recognition*, pp. 12275–12284, 2020b.
- Weiler, M. and Cesa, G. General E (2)-equivariant steerable CNNs. *Advances in Neural Information Processing Systems*, 32, 2019.
- Weiler, M., Geiger, M., Welling, M., Boomsma, W., and Cohen, T. S. 3D steerable CNNs: Learning rotationally equivariant features in volumetric data. *Advances in Neural Information Processing Systems*, 31, 2018a.
- Weiler, M., Hamprecht, F. A., and Storath, M. Learning steerable filters for rotation equivariant CNNs. In *Proceedings of the IEEE Conference on Computer Vision and Pattern Recognition*, pp. 849–858, 2018b.
- Winkels, M. and Cohen, T. S. Pulmonary nodule detection in CT scans with equivariant CNNs. *Medical image analysis*, 55:15–26, 2019.

- Xie, X., Zhou, P., Li, H., Lin, Z., and Yan, S. Adan: Adaptive Nesterov momentum algorithm for faster optimizing deep models. *IEEE Transactions on Pattern Analysis and Machine Intelligence*, 2024.
- Xu, K., Chen, L., and Wang, S. Kolmogorov-Arnold networks for time series: Bridging predictive power and interpretability. *arXiv preprint arXiv:2406.02496*, 2024.
- Yu, R., Yu, W., and Wang, X. KAN or MLP: A fairer comparison. *arXiv preprint arXiv:2407.16674*, 2024.
- Zaheer, M., Kottur, S., Ravanbakhsh, S., Poczos, B., Salakhutdinov, R. R., and Smola, A. J. Deep sets. *Advances in Neural Information Processing Systems*, 30, 2017.
- Zhang, F. and Zhang, X. GraphKAN: Enhancing feature extraction with graph Kolmogorov Arnold networks. *arXiv preprint arXiv:2406.13597*, 2024.
- Zhao, L., Zhu, X., Kong, L., Walters, R., and Wong, L. L. Integrating symmetry into differentiable planning with steerable convolutions. *arXiv preprint arXiv:2206.03674*, 2022.

A. Common matrix groups and their generators

A.1. Groups $SO(2)$ and $O(2)$

The group $SO(2)$ represents rotation transformations in two-dimensional space. Its group elements can be expressed as:

$$R(\theta) = \begin{bmatrix} \cos \theta & -\sin \theta \\ \sin \theta & \cos \theta \end{bmatrix}. \quad (21)$$

It corresponds to an infinitesimal generator:

$$A_1 = \begin{bmatrix} 0 & -1 \\ 1 & 0 \end{bmatrix}. \quad (22)$$

Then we can obtain the group elements through the exponential map $R(\theta) = \exp(\theta A_1)$.

The group $O(2)$ represents orthogonal transformations in two-dimensional space, including rotations and reflections. Based on the group $SO(2)$, it has an additional discrete generator:

$$h_1 = \begin{bmatrix} 1 & 0 \\ 0 & -1 \end{bmatrix}. \quad (23)$$

A.2. Groups $SO^+(1, 3)$, $SO(1, 3)$, and $O(1, 3)$

The group $SO^+(1, 3)$ represents Lorentz transformations that preserve both orientation and the direction of time. It includes six infinitesimal generators:

$$\begin{cases} A_1 = \begin{bmatrix} 0 & 1 & 0 & 0 \\ 1 & 0 & 0 & 0 \\ 0 & 0 & 0 & 0 \\ 0 & 0 & 0 & 0 \end{bmatrix}, A_2 = \begin{bmatrix} 0 & 0 & 1 & 0 \\ 0 & 0 & 0 & 0 \\ 1 & 0 & 0 & 0 \\ 0 & 0 & 0 & 0 \end{bmatrix}, A_3 = \begin{bmatrix} 0 & 0 & 0 & 1 \\ 0 & 0 & 0 & 0 \\ 0 & 0 & 0 & 0 \\ 1 & 0 & 0 & 0 \end{bmatrix}, \\ A_4 = \begin{bmatrix} 0 & 0 & 0 & 0 \\ 0 & 0 & 1 & 0 \\ 0 & -1 & 0 & 0 \\ 0 & 0 & 0 & 0 \end{bmatrix}, A_5 = \begin{bmatrix} 0 & 0 & 0 & 0 \\ 0 & 0 & 0 & 1 \\ 0 & 0 & 0 & 0 \\ 0 & -1 & 0 & 0 \end{bmatrix}, A_6 = \begin{bmatrix} 0 & 0 & 0 & 0 \\ 0 & 0 & 0 & 0 \\ 0 & 0 & 0 & 1 \\ 0 & 0 & -1 & 0 \end{bmatrix}, \end{cases} \quad (24)$$

where A_1, A_2, A_3 correspond to Lorentz boosts, and A_4, A_5, A_6 correspond to spatial rotations.

The group $SO(1, 3)$ represents Lorentz transformations that preserve orientation. Based on the group $SO^+(1, 3)$, it has an additional discrete generator:

$$h_1 = \begin{bmatrix} -1 & 0 & 0 & 0 \\ 0 & -1 & 0 & 0 \\ 0 & 0 & -1 & 0 \\ 0 & 0 & 0 & -1 \end{bmatrix}, \quad (25)$$

which corresponds to orientation reversal.

The group $O(1, 3)$ represents all Lorentz transformations. Based on the group $SO(1, 3)$, it has an additional discrete generator:

$$h_2 = \begin{bmatrix} -1 & 0 & 0 & 0 \\ 0 & 1 & 0 & 0 \\ 0 & 0 & 1 & 0 \\ 0 & 0 & 0 & 1 \end{bmatrix}, \quad (26)$$

which corresponds to time reversal.

B. Equivariant Multi-Layer Perceptrons (EMLP)

EMLP (Finzi et al., 2021) embeds matrix group equivariance into MLPs layerwise. Given the input space U_i and output space U_o , the linear weight matrix $W \in U_o \otimes U_i^*$ should satisfy Equation (5), i.e., $\forall g \in \tilde{G}, v_i \in U_i : \rho_o(g)Wv_i = W\rho_i(g)v_i$. So

the coefficients of each term in v_i are equal $\forall g \in \tilde{G} : \rho_o(g)W = W\rho_i(g)$. Flattening the linear weight matrix W into a vector, we have $\forall g \in \tilde{G} : [\rho_o(g) \otimes \rho_i(g^{-1})^\top] \text{vec}(W) = \text{vec}(W)$. Combined with Equation (4), the linear weight matrix W is invariant in the space $U_o \otimes U_i^*$:

$$\forall g \in \tilde{G} : \rho_{o,i}(g) \text{vec}(W) = \text{vec}(W), \quad (27)$$

where $\rho_{o,i} = \rho_o \otimes \rho_i^*$ is the group representation of $U_o \otimes U_i^*$. Decomposing the group representation $\rho_{o,i}(g)$ into discrete and infinitesimal generators as shown in Equation (2), Equation (27) is equivalent to the following constraint:

$$C \text{vec}(W) = \begin{bmatrix} d\rho_{o,i}(A_1) \\ \vdots \\ d\rho_{o,i}(A_D) \\ \rho_{o,i}(h_1) - I \\ \vdots \\ \rho_{o,i}(h_M) - I \end{bmatrix} \text{vec}(W) = 0. \quad (28)$$

By performing singular value decomposition (SVD) on the coefficient matrix C , we can obtain its nullspace, which corresponds to the subspace where the equivariant linear weights reside.

C. Proof of Theorem 4.1

Theorem 4.1. *Given a matrix group \tilde{G} , the gated input space U_{gi} and the post-activation space U_m can be expressed in the forms of Equations (9) and (13), respectively. The function $f : U_{gi} \rightarrow U_m$ is defined by Equations (10) to (12), that is, $v_m = f(v_{gi})$. Then, f is equivariant:*

$$\forall g \in \tilde{G}, v_{gi} \in U_{gi} : \rho_m(g)f(v_{gi}) = f(\rho_{gi}(g)v_{gi}), \quad (14)$$

where ρ_{gi} and ρ_m are group representations of U_{gi} and U_m , respectively.

Proof. Let $v_{m,b} = f_b(v_{gi})$, then Equation (11) can be written as:

$$f(v_{gi}) = \bigoplus_{b=0}^{G+k} f_b(v_{gi}). \quad (29)$$

Using the structure of U_m shown in Equation (13) and applying the rules from Equation (4), we can derive the group representation of U_m :

$$\rho_m(g) = \bigoplus_{b=0}^{G+k} \rho_i(g), \quad (30)$$

where ρ_i is the group representation of U_i . Combining Equations (29) and (30), we have:

$$\rho_m(g)f(v_{gi}) = \bigoplus_{b=0}^{G+k} \rho_i(g)f_b(v_{gi}). \quad (31)$$

Note that the group transformation in the scalar space T_0 is the identity transformation, then we can obtain the group representation of U_{gi} from Equation (9):

$$\rho_{gi}(g) = I_{c_i} \oplus \left[\bigoplus_{a=1}^{A_i} \rho_{i,a}(g) \right] \oplus I_{A_i}, \quad (32)$$

where $\rho_{i,a}$ is the group representation of $T(p_{i,a}, q_{i,a})$. Therefore, applying the group transformation to v_{gi} in Equation (10) results in:

$$\rho_{gi}(g)v_{gi} = \left(\bigoplus_{a=1}^{c_i} s_{i,a} \right) \oplus \left(\bigoplus_{a=1}^{A_i} \rho_{i,a}(g)v_{i,a} \right) \oplus \left(\bigoplus_{a=1}^{A_i} s'_{i,a} \right). \quad (33)$$

Substitute Equation (33) into Equation (12):

$$f_b(\rho_{gi}(g)v_{gi}) = \begin{cases} [\bigoplus_{a=1}^{c_i} s_{i,a} B_b(s_{i,a})] \oplus [\bigoplus_{a=1}^{A_i} \rho_{i,a}(g) v_{i,a} B_b(s'_{i,a})], & b < G + k, \\ [\bigoplus_{a=1}^{c_i} s_{i,a} \text{silu}(s_{i,a})] \oplus [\bigoplus_{a=1}^{A_i} \rho_{i,a}(g) v_{i,a} \text{silu}(s'_{i,a})], & b = G + k. \end{cases} \quad (34)$$

Similar to Equation (32), we can derive the group representation of U_i from Equation (8):

$$\rho_i(g) = I_{c_i} \oplus \left[\bigoplus_{a=1}^{A_i} \rho_{i,a}(g) \right]. \quad (35)$$

Note that the right-hand side of Equation (34) is the result of applying $\rho_i(g)$ to $f_b(v_{gi})$, which means:

$$f_b(\rho_{gi}(g)v_{gi}) = \rho_i(g) f_b(v_{gi}). \quad (36)$$

Substitute Equation (36) into Equation (29):

$$f(\rho_{gi}(g)v_{gi}) = \bigoplus_{b=0}^{G+k} \rho_i(g) f_b(v_{gi}). \quad (37)$$

Combining Equations (31) and (37), Equation (14) is proven. \square

D. Grid update

Similar to KANs (Liu et al., 2024b), EKAN updates grids based on the input activations. At the same time, the linear weights should also be updated in order to keep the output features unchanged. Let the post-activation values of the grids before and after the update be denoted as $V_m, V'_m \in \mathbb{R}^{N \times (G+k+1)d_i}$, where N is the number of samples. We first project the linear weight blocks into the equivariant subspace as $\text{vec}(\widetilde{W}_b) = P \text{vec}(W_b)$ and compute the output activations $V_{go} = V_m \widetilde{W}^\top = \sum_{b=0}^{G+k} V_{m,b} \widetilde{W}_b^\top$, where P is the equivariant projector obtained from Equation (20). Then, the updated equivariant linear weights \widetilde{W}' should satisfy $V_{go} = V'_m \widetilde{W}'^\top$, and we have $\widetilde{W}' = V_{go}^\top (V'_m{}^\top)^\dagger$. We finally restore the updated linear weight blocks $\text{vec}(W'_b) = P^\dagger \text{vec}(\widetilde{W}'_b)$.

E. Implementation details

E.1. Particle scattering

In particle scattering, we generate training sets of different sizes, and the corresponding test sets have the same sizes as the training sets. We train EKAN using the Adan optimizer (Xie et al., 2024) with the learning rate of 3×10^{-3} and the batch size of 500. For datasets with the training set size < 1000 , we set the number of epochs to 7000, while for datasets with the training set size ≥ 1000 , we set the number of epochs to 15000, which is sufficient for the MSE loss to converge to the minimum. We perform this experiment on a single-core NVIDIA GeForce RTX 3090 GPU with available memory of 24576 MiB.

E.2. Three-body problem

In the three-body problem, we control the number of parameters by adjusting the middle layer width N of the model. We list the correspondence between the model's shape and the number of parameters in Table 4. We train all models using the Adan optimizer (Xie et al., 2024) with the learning rate of 3×10^{-3} , the batch size of 500, and for 5000 epochs. The grids of EKAN and KAN are updated every 5 epochs and stop updating at the 50th epoch. We perform this experiment on a single-core NVIDIA GeForce RTX 3090 GPU with available memory of 24576 MiB.

E.3. Top quark tagging

In top quark tagging, we train all models using the Adan optimizer (Xie et al., 2024) with the learning rate of 3×10^{-3} and the batch size of 500. For datasets with the training set size ≤ 1000 , we set the number of epochs to 1000, while for datasets with the training set size > 1000 , we set the number of epochs to 2000, which is sufficient for the BCE loss to converge to the minimum. The grids of EKAN and KAN are updated every 5 epochs and stop updating at the 50th epoch. We perform this experiment on a single-core NVIDIA GeForce RTX 3090 GPU with available memory of 24576 MiB.

Table 4. The correspondence between the model’s shape and the number of parameters.

Models	Number of parameters				
	$10^{4.5}$	$10^{4.75}$	10^5	$10^{5.25}$	$10^{5.5}$
MLP	[48, 111, 111, 111, 12]	[48, 153, 153, 153, 12]	[48, 209, 209, 209, 12]	[48, 283, 283, 283, 12]	[48, 383, 383, 383, 12]
EMLP	[48, 84, 84, 84, 12]	[48, 110, 110, 110, 12]	[48, 147, 147, 147, 12]	[48, 214, 214, 214, 12]	[48, 281, 281, 281, 12]
KAN	[48, 76, 12]	[48, 134, 12]	[48, 238, 12]	[48, 423, 12]	[48, 752, 12]
EKAN (Ours)	[48, 45, 12]	[48, 88, 12]	[48, 151, 12]	[48, 262, 12]	[48, 457, 12]